

# Unfocused Field Analysis of a Density-Tapered Spiral Array for High-Volume-Rate 3-D Ultrasound Imaging

Rebekah Maffett<sup>1b</sup>, *Graduate Student Member, IEEE*, Enrico Boni<sup>1b</sup>, *Senior Member, IEEE*,  
 Adrian J. Y. Chee, *Member, IEEE*, Billy Y. S. Yiu<sup>1b</sup>, *Member, IEEE*,  
 Alessandro Stuart Savoia<sup>1b</sup>, *Member, IEEE*, Alessandro Ramalli<sup>1b</sup>, *Senior Member, IEEE*,  
 Piero Tortoli<sup>1b</sup>, *Fellow, IEEE*, and Alfred C. H. Yu<sup>1b</sup>, *Senior Member, IEEE*

**Abstract**—Spiral array transducers with a sparse 2-D aperture have demonstrated their potential in realizing 3-D ultrasound imaging with reduced data rates. Nevertheless, their feasibility in high-volume-rate imaging based on unfocused transmissions has yet to be established. From a metrology standpoint, it is essential to characterize the acoustic field of unfocused transmissions from spiral arrays not only to assess their safety but also to identify the root cause of imaging irregularities due to the array's sparse aperture. Here, we present a field profile analysis of unfocused transmissions from a density-tapered spiral array transducer (256 hexagonal elements, 220- $\mu\text{m}$  element diameter, and 1-cm aperture diameter) through both simulations and hydrophone measurements. We investigated plane- and diverging-wave transmissions (five-cycle, 7.5-MHz pulses) from 0° to 10° steering for their beam intensity characteristics and wavefront arrival time profiles. Unfocused firings were also tested for B-mode imaging performance (ten compounded angles,  $-5^\circ$  to  $5^\circ$  span). The array was found to produce unfocused transmissions with a peak negative pressure of 93.9 kPa at 2 cm depth. All transmissions steered up to 5° were free of secondary lobes within 12 dB of the main beam peak intensity. All wavefront arrival time profiles were found to closely match the expected profiles with maximum root-mean-squared errors of 0.054  $\mu\text{s}$  for plane wave (PW) and 0.124  $\mu\text{s}$  for diverging wave. The

B-mode images showed good spatial resolution with a penetration depth of 22 mm in PW imaging. Overall, these results demonstrate that the density-tapered spiral array can facilitate unfocused transmissions below regulatory limits (mechanical index: 0.034; spatial-peak, pulse-average intensity: 0.298 W/cm<sup>2</sup>) and with suppressed secondary lobes while maintaining smooth wavefronts.

**Index Terms**—3-D imaging, acoustic field profile, high volume rate, sparse arrays.

## I. INTRODUCTION

**D**YNAMIC 3-D ultrasound imaging has demonstrated potential in tracking physiological events such as blood flow on a time-resolved basis [1], [2]. However, the development of dynamic 3-D ultrasound methods is dependent on high-volume-rate acquisitions [e.g., 1000 volumes per second (vps)] that cannot be realized using conventional 3-D imaging strategies based on mechanical scanning, as these strategies typically yield volume rates below 1 vps. The advent of 2-D matrix arrays has been a major step in this field that increased volume rates significantly over the physical scanning of linear arrays (from  $<1$  to  $\sim 10$  vps) [3], [4]; yet, the volume rate remains too low to image dynamic flow events within a single cardiac cycle if traditional scanline (focused beam) imaging is used [5]. To address the volume rate limitations of 3-D scanline methods, unfocused transmission schemes developed in 2-D ultrasound [6], [7] could potentially be extended into the 3-D imaging space. Unfocused transmissions have enabled 2-D ultrasound imaging at rates of 10000 frames/s through the insonification of the full imaging view on each firing. Nevertheless, the extension of unfocused transmission schemes from 1-D arrays to 2-D matrix arrays is nontrivial given the immense increase in element count.

A 2-D matrix array typically contains over 1000 transducer elements (e.g., [8]) that correspond to high channel counts as well as high pre-beamformed data rates. The costs of using 2-D matrix arrays become especially apparent in unfocused imaging schemes where all elements are receiving data simultaneously. The corresponding data rates on 2-D matrix arrays can easily exceed 50 GB/s depending on the

Manuscript received 1 May 2022; accepted 29 June 2022. Date of publication 4 July 2022; date of current version 27 September 2022. This work was supported in part by the Natural Sciences and Engineering Council of Canada under Grant CREATE-528202-2019 and Grant RGPIN-2022-04157, in part by the E.W.R. Steacie Memorial Fellowship under Grant SMFSU-556263-2021, in part by the Canadian Space Agency under Grant 21FAWATA08, and in part by the Moore4Medical platform funded by the ECSEL Joint Undertaking Grant H2020-ECSEL-2019-IA-876190. (Corresponding author: Alfred C. H. Yu.)

Rebekah Maffett, Adrian J. Y. Chee, Billy Y. S. Yiu, and Alfred C. H. Yu are with the Schlegel Research Institute for Aging and the Department of Electrical and Computer Engineering, University of Waterloo, Waterloo, ON N2L 3G1, Canada (e-mail: alfred.yu@uwaterloo.ca).

Enrico Boni, Alessandro Ramalli, and Piero Tortoli are with the Department of Information Engineering, University of Florence, 50139 Florence, Italy.

Alessandro Stuart Savoia is with the Department of Industrial, Electronic, and Mechanical Engineering, Roma Tre University, 00146 Rome, Italy.

This article has supplementary material provided by the authors and color versions of one or more figures available at <https://doi.org/10.1109/TUFFC.2022.3188245>.

Digital Object Identifier 10.1109/TUFFC.2022.3188245

acquisition parameters (i.e., pulse repetition frequency and sampling rate). Such high data rates are not manageable by clinical or research ultrasound scanners (e.g., Verasonics or ULA-OP 256 [9]) without hardware modifications, thereby rendering high-volume-rate 3-D ultrasound investigations with 2-D matrix arrays unattainable except on highly specialized and bulky systems [8], [10]. To make high-volume-rate ultrasound studies available for the wider research community, data rate reduction strategies must be developed to eliminate the need for expensive scanner hardware modifications. A more economical approach is to reduce the data rates directly from the probe rather than altering the scanner. Currently, there are two proposed solutions that reduce data rates directly on the probe: row-column addressing (RCA) and sparse arrays. RCA arrays maintain the element density of 2-D matrix arrays and reduce channel counts via crossed electrodes where only entire rows and columns can be addressed at a time [11], [12]. However, RCA prevents full 3-D steering and halves the maximum volume rate [1]. Sparse arrays instead reduce the element density to reduce the channel counts. This latter type of 2-D array is not subjected to constraints in 3-D steering and volume rate that are faced by RCA arrays.

In general, 2-D sparse arrays have the potential in realizing high-volume-rate 3-D ultrasound imaging. Yet, the beam degradation arising from exceeding a  $\lambda/2$  element spacing may hinder the ability of sparse arrays to produce accurate flow measurements. Therefore, for sparse arrays to truly be suitable for high-volume-rate 3-D ultrasound, the arrays must be appropriately designed so that they can produce high-quality field transmission profiles. Many studies have focused on optimizing the layout of sparse arrays using *in silico* methods [13]–[20]. To robustly assess the performance of prototype sparse arrays in a range of transmission conditions, direct field profile measurements should be acquired. Such measurements will allow researchers to mitigate imaging irregularities stemming from nonideal beam profiles in any imaging mode. They are also important to exposure safety assessments in determining whether the generated acoustic intensities are within regulatory limits, such as those set forth by the Food and Drug Administration (FDA) [21].

In this work, we assess the acoustic field performance and the safety of a spiral array transducer with a sparse 2-D aperture to determine whether it can properly support the realization of high-volume-rate 3-D ultrasound imaging. Specifically, we evaluate the field profiles of unfocused transmissions (both plane and diverging waves) from a density-tapered spiral array, which has demonstrated high-quality focused beam characteristics *in silico* [19] and *in vitro* [22] but has yet to be investigated for unfocused beam transmissions. In addition, we examine the surface temperature of the array to evaluate its safety for future *in vivo* studies. The physical array studied in this work is a density-tapered spiral array design that preserves the nongridded and nonsymmetric layout, and it was realized through a capacitive micromachined ultrasound transducer (CMUT) fabrication approach [22]. We posit that the transmission characteristics of the spiral array, such as beam intensity and arrival time profile, will be preserved in unfocused transmission modes. The field profile analysis,

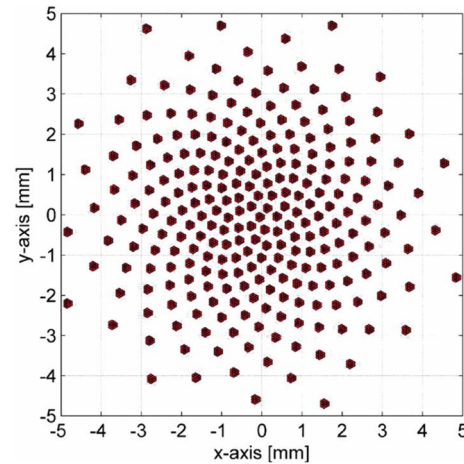


Fig. 1. Layout of the physical CMUT density tapered spiral array with hexagonal elements.

performed both *in silico* and *in vitro*, will examine both steered and unsteered transmissions over a range of depths relevant to peripheral vascular imaging *in vivo*. This study serves to lay the groundwork for future applications of the density-tapered spiral array as a viable transducer configuration for high-volume-rate 3-D ultrasound imaging of physiological dynamics.

## II. EXPERIMENTAL METHODS

The rationale for performing both hydrophone measurements and field profile simulations in this study is twofold. First, hydrophone measurements can directly assess the true transmission properties of an array, whereas simulations provide reference profiles to ensure that there is no systemic error from the experimental setup. Second, direct field profile measurements will be subject to nonidealities of the array (e.g., nonuniform element excitations and sensitivity), whereas simulation results have idealized array performance, which provides a theoretical base for the hydrophone measurements.

The density-tapered spiral array used in this study is a CMUT array with 256 elements [19], [22]. It has a two-way  $-6$ -dB bandwidth centered at 7 MHz. The array, shown in Fig. 1, has hexagonal elements with a diameter of  $220 \mu\text{m}$  where each element is composed of 19 circular subelements. The elements follow a Blackman window-based density tapering with the center and edges of the array containing, respectively, the highest and lowest element spatial density. This type of density tapering is used here since it was found to have a favorable performance tradeoff (in focused beam simulations) between various parameters, including lateral resolution, grating lobe levels, and effective aperture for small vessel imaging compared to other density tapering functions of the Fermat spiral [19]. The total footprint of the array is a circular surface with a 1 cm diameter. With density tapering, the effective array diameter is 0.6 cm.

Three types of unfocused transmissions were studied: 1) plane wave (PW); 2) diverging wave with a virtual point source 30 mm behind the array (DIV30); and 3) diverging wave with a virtual point source 20 mm behind the array (DIV20). Every pulsing event involved the use of a five-cycle, 7.5-MHz sinusoidal pulse with a 20% Tukey window. The

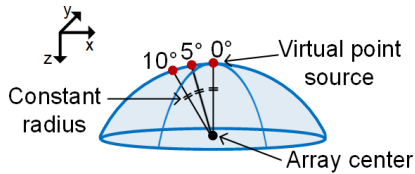


Fig. 2. Schematic of diverging wave steering. Virtual point sources are shifted on the surface of a sphere centered at the center of the array to maintain a constant degree of divergence with steering.

TABLE I  
TRANSMISSION, MEASUREMENT, AND MEDIUM PROPERTIES

Parameter	Experimental Setup	Simulation
Center frequency	7.5 MHz	
Pulse shape	5-cycle sinusoid	
Window	20% Tukey	
Sampling frequency	100 MHz	
Speed of sound	~1480 m/s (degassed water)	1480 m/s
Wavelength	~197.3 $\mu\text{m}$	
Attenuation	~0 dB/cm·MHz	0 dB/cm·MHz
Spatial sample spacing	100 $\mu\text{m}$ ( $\sim\lambda/2$ ) or 200 $\mu\text{m}$ ( $\sim\lambda$ )	50 $\mu\text{m}$ ( $\sim\lambda/4$ )
Spatial averaging	0.13 mm <sup>2</sup>	0 $\mu\text{m}^2$

pulse parameters were selected to generate the typical pulse used for pulsed Doppler measurements. The array was biased at 75 V (the maximum voltage without damaging the array elements), and a working voltage of 20 V peak-to-peak was used for all transmissions. No transmit apodization was applied on the array since the density tapering serves as a physical apodization. The DIV30 and DIV20 firings were studied at transmission angles of 0°, 5°, and 10° with the virtual point source maintaining a constant distance from the center of the array (see Fig. 2). The PW firings were studied at transmission angles of 1°, 5°, and 10°; 0° was not studied because it caused unexpected behavior of the pulsers due to the high peak current required during the simultaneous firing of all 256 elements. The range of steering angles studied in this work was an empirical parameter choice that was made based on previous studies that often used an angle span of 20° (i.e., from  $-10^\circ$  to  $+10^\circ$ ) for multi-angle Doppler estimation [23]. Complete transmission specifications are listed in Table I.

The pressure field profile was acquired over two planes perpendicular to the probe surface and three planes parallel. The perpendicular planes, one on the XZ plane and one on the YZ plane, had a width of two times the theoretical maximum main beamwidth in the X- and Y-directions. They each spanned from 20 to 60 mm depth in the Z-direction [see Fig. 3(a)]; this range in depths of the measurement planes was set to match the typical depths used in peripheral vascular imaging (e.g., brachial and carotid). The remaining three acquisition planes were parallel to the probe surface on XY planes at depths of 20, 40, and 60 mm and were sized to match the maximum main beamwidth as well as centered with the main beam [see Fig. 3(b)].

### A. Hydrophone Measurements

Hydrophone measurements were performed in a degassed water tank (20 °C, ~1480 m/s) with an attached three-axis motion stage (IntelLiDrives, Inc., Philadelphia, PA, USA). The

motion stage has a 20- $\mu\text{m}$  motion resolution on all three axes and was controlled by a personal computer. An Onda HGL-400 capsule hydrophone (Onda Corporation, Sunnyvale, CA, USA) was mounted on the motion stage and was immersed in the water tank [see Fig. 3(c)]. The hydrophone was oriented such that the measurement surface was directed upward toward the array surface. This model of hydrophone has an aperture of 400  $\mu\text{m}$  resulting in spatial averaging of the measurements at each point. The hydrophone was connected to an AH-2010-100 preamplifier (Onda Corporation, Sunnyvale, CA, USA) and the signal was routed to a Rigol DS1104 oscilloscope (Rigol, Portland, OR, USA) that sampled at 100 MHz. The same personal computer controlling the motion stage was used to read the hydrophone acquisitions from the oscilloscope.

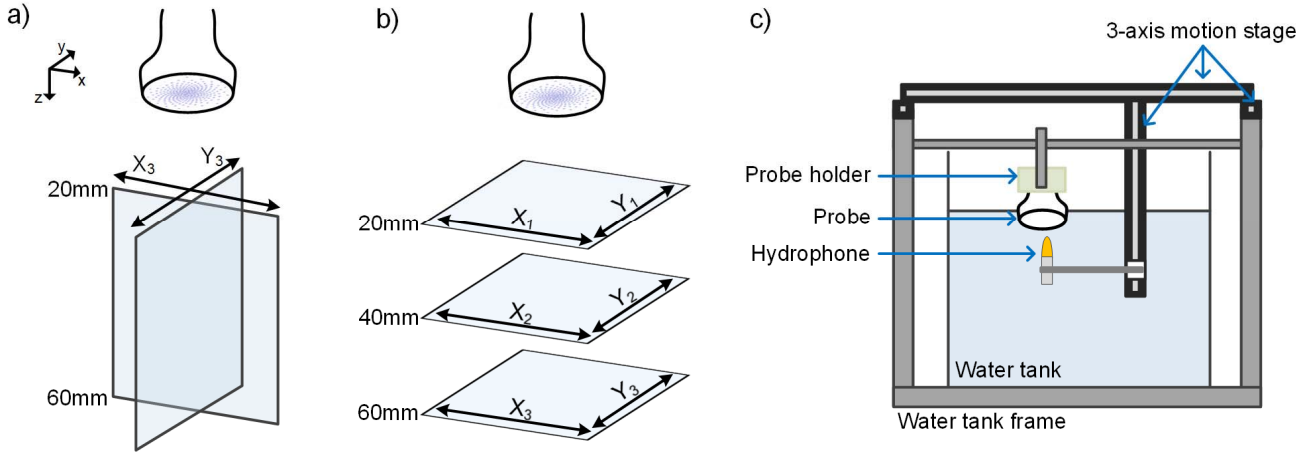
The density-tapered spiral array was mounted on the water tank frame using a custom 3-D printed probe holder and was placed in the scan tank with the array pointing downward [see Fig. 3(c)]. The probe orientation thus had a fixed alignment with the frame of the water tank. The surface of the array was located <5 mm below the surface of the water. The array was driven by a ULA-OP 256 research ultrasound scanner [9] with a CMUT adapter board. A sync output from the scanner was also connected to the oscilloscope to provide a trigger for the hydrophone measurements. The scanner was controlled through a second personal computer where the transmission profiles were programmed.

With the array and hydrophone in place in the scan tank, the hydrophone was moved underneath the array. The origin of the XY scan planes for the hydrophone was set at the center of the array using a focused beam transmission from the array. Using increasingly fine step sizes, the hydrophone could be placed at the peak of the transmission with 50- $\mu\text{m}$  accuracy. For steered transmissions, the origin was moved in the X- or Y-directions from the array center to the center of the steered beam. To set the desired depth of the hydrophone below the array, the time between the trigger pulse and the recorded wave on the hydrophone was measured on the oscilloscope. The time between the pulses (after subtracting a fixed transmission delay value) was multiplied by the speed of sound in the water, 1480 m/s, to yield the depth of the hydrophone below the array. The depth of the array was accurate to 50  $\mu\text{m}$ .

To record the field profile of various transmissions, the hydrophone was stepped over a 2-D grid on the desired plane. For acquisition planes up to 9 cm<sup>2</sup> in area, a step size of 100  $\mu\text{m}$  ( $\lambda/2$ ) was used. For all larger acquisition planes, step sizes of 200  $\mu\text{m}$  ( $\lambda$ ) were used for intensity and arrival time analysis.

### B. Field Profile Simulations

Simulations of the pressure field profile from the density tapered spiral array were performed in MATLAB (MathWorks, Natick, MA, USA) using Field II [24], [25]. The simulated array contained 256 square elements with a 200  $\mu\text{m}$  width in the same locations as the physical spiral array. The element size between simulation and the physical array is similar since a 220- $\mu\text{m}$ -diameter hexagon when measured from corner to opposite corner has a 200  $\mu\text{m}$  width measured from



**Fig. 3.** (a) Acquisition planes on the XZ and YZ planes where the width in  $X_3$  is two times the theoretical beamwidth at 60 mm depth. (b) Acquisition planes on XY planes where the widths  $X_{1,2,3}$  and  $Y_{1,2,3}$  are defined by the theoretical beamwidth at each depth. (c) Schematic of the hydrophone measurement setup with the hydrophone mounted to the three-axis motion stage and the spiral array mounted to the water tank frame.

side to opposite side. The simulated transmissions were set identically to the experimental transmissions and the simulated medium was set to match the properties of water. Unlike the hydrophone measurements, the simulated data points have no spatial averaging. All other key simulation parameters are listed in Table I.

### C. Intensity Analysis

The peak absolute pressure at each point on the acquisition planes was extracted and converted to decibels to yield the intensity of the point. The XZ and YZ planes were used to observe the beam properties across depth while also identifying secondary lobes outside of the main beam. In this work, secondary lobes are considered to be regions outside the main beam with an intensity close to the main beam intensity (e.g., greater than one-quarter of the main beam intensity). Their emergence may be attributed to grating lobes and sidelobes in the field profile. They were identified by applying a  $-12$ -dB intensity threshold relative to the main beam peak on each XZ and YZ plane. The XY planes were used to study the radial properties of the beam.

### D. Arrival Time Analysis

The XZ and YZ planes were used to observe the propagation of the generated wavefront across depth. A cineloop of the wavefront propagation across depth can be formed by stepping sample-by-sample on all acquisition points on the XZ and YZ planes simultaneously and saving each sample time as a video frame. On the XY planes, the wavefront arrival time can be calculated at each acquisition point by computing the lag of the maximum cross correlation between the excitation pulse and the measured waveform. To evaluate the main beam arrival time performance, the wavefront arrival time profiles in experiments and simulations were compared to an expected profile for the transmission. For PWs, the expected profile is simply a plane that matches the steering angle. For diverging waves, the expected profile takes the form of a hyperboloid.

Specifically, for a given spatial point in front of the array aperture  $(x_o, y_o, z_o)$  and a virtual point source location  $(x_{vp}, y_{vp}, z_{vp})$ , the arrival time  $t$  of a diverging wavefront can be theoretically calculated from the following equation:

$$t^2 = \left( \frac{x_o - x_{vp}}{c} \right)^2 + \left( \frac{y_o - y_{vp}}{c} \right)^2 + \left( \frac{z_o - z_{vp}}{c} \right)^2 \quad (1)$$

where  $c$  is the speed of sound. The root-mean-squared error (RMSE) between the expected and acquired arrival time profiles was accordingly calculated for both simulations and experiments.

### E. In Vitro B-Mode Imaging

Unfocused B-mode imaging performance of the array was assessed using two phantoms: 1) CIRS Multi-Purpose Multi-Tissue Ultrasound Phantom (CIRS, Inc., Norfolk, VA, USA) with an attenuation of  $0.3 \text{ dB/cm} \cdot \text{MHz}$  and 2) an in-house fabricated wire target phantom immersed in water ( $100\text{-}\mu\text{m}$  tungsten wires aligned axially spaced  $1 \text{ cm}$  apart). Wire targets in both phantoms were imaged with the  $y$ -axis of the spiral array aligned parallel with the line targets. PW and DIV20 firings (the least- and most-divergent firings) were used with ten transmission angles spanning from  $-5^\circ$  to  $5^\circ$  on the  $x$ -axis, omitting  $0^\circ$ , with no steering on the  $y$ -axis. A 3-D GPU-based delay-and-sum beamformer, essentially an extended version of the 2-D GPU beamformer [26], was used to form the images for each transmission angle followed by coherent compounding of all angles. The resulting images were assessed for their penetration depth and spatial resolution. The penetration depth in the CIRS phantom was assessed qualitatively by observing at which depth the targets became indistinguishable from the surrounding speckle pattern. The spatial resolution was calculated from the full-width at half-maximum (FWHM) of the point targets in the  $x$ - and  $z$ -axes of the images of both phantoms. The average sidelobe level (SLL) was evaluated on the images from the water phantom on the ZX plane. The SLL was extracted from lateral positions of  $x < -1.5 \text{ mm}$  and  $x > 1.5 \text{ mm}$  (to exclude the point target)

and over an axial range from 5 pixels above the point target depth to the depth of the point target (to include the upward curving nature of the sidelobes). The average SLL for each point target was then normalized to the peak intensity of the point target.

#### F. Probe Surface Temperature Measurements

Surface temperature measurements on the array were acquired in accordance with the International Electrotechnical Commission (IEC) standard protocol (IEC 60601-2-37). In brief, a tissue-mimicking phantom made from a poly(vinyl)-alcohol hydrogel was immersed in a 33 °C water bath for 1 h. Then, with the phantom still in the water bath, the probe was placed on the phantom surface. The probe was set to transmit a DIV20 transmission without steering at 5-kHz PRF for 30 min, after which an infrared camera (TG165, Teledyne FLIR, Wilsonville, OR, USA) was used to measure the temperature of the array surface. A final surface temperature of 43 °C or less is considered safe for external *in vivo* use of an ultrasound array.

### III. RESULTS

#### A. Spiral Array Produces High-Quality Beam Profiles for Unfocused Firings

The density-tapered spiral array had measured peak negative pressures (PNPs) of 93.9, 59.3, and 45.6 kPa for PW, DIV30, and DIV20, respectively. Fig. 4(a)–(i) shows the intensity of the XZ planes measured by the hydrophone. The left, center, and right columns, respectively, show the XZ planes for PW, DIV30, and DIV20 firings, whereas the top, middle, and bottom rows, respectively, show the XZ planes at the steering angle of 0°/1°, 5°, and 10°. The inset figure on each XZ plane is a binary map with a –12-dB threshold from the main beam peak applied. Overall, Fig. 4 shows the intensity profiles across all transmission types. The PW firings show a consistent beamwidth across depth, while the DIV30 and DIV20 firings expand across depth as expected. The presence of secondary lobes in all firings is apparent from the intensity profiles; however, only a few of them are within the –12-dB threshold (i.e., higher than one-quarter) of the main beam intensity. Fig. 4(j) and (l) shows an intensity cross-sectional plot taken at a depth of 40 mm and overlaid for each steering angle of the same transmission type. These plots highlight the secondary lobe levels compared to the main lobe. For PW [Fig. 4(j)], the main lobe-to-secondary lobe ratio is 24.84 dB for 1° steering and 14.26 dB for 10° steering; for DIV30 [Fig. 4(k)], it is 18.67 dB for 0° and 6.74 dB for 10°; and for DIV20 [Fig. 4(l)], it is 18.45 dB for 0° and 14.40 dB for 10°. While not explicitly shown here for brevity, the array performed similarly between the *x*- and *y*-axis steering.

Fig. 5(a)–(c) shows the XY plane of the 1° PW, 0° DIV30, and 0° DIV20 firings, respectively, at a depth of 40 mm as measured by the hydrophone. Fig. 5(d)–(f) shows the same planes from the simulated results. Here, the radial beam characteristics of the array can be observed and compared to the ideal performance of the simulated array. The simulated results show a uniform radial performance since each element

is transmitting at identical amplitudes. The physical array has some beam imperfections resulting in a less uniform radial performance [e.g., Fig. 5(a) has a less circular intensity pattern than Fig. 5(d)]. On all XY planes in simulation and hydrophone measurements, there are no direction-dependent beam patterns and the main beams are relatively circular in nature. However, there is a notable difference in intensity between the hydrophone and simulated results, especially toward the outer edges of the main beam where the simulations show a much higher intensity than the hydrophone measurements.

#### B. Wavefronts Generated From the Spiral Array Match the Expected Profiles




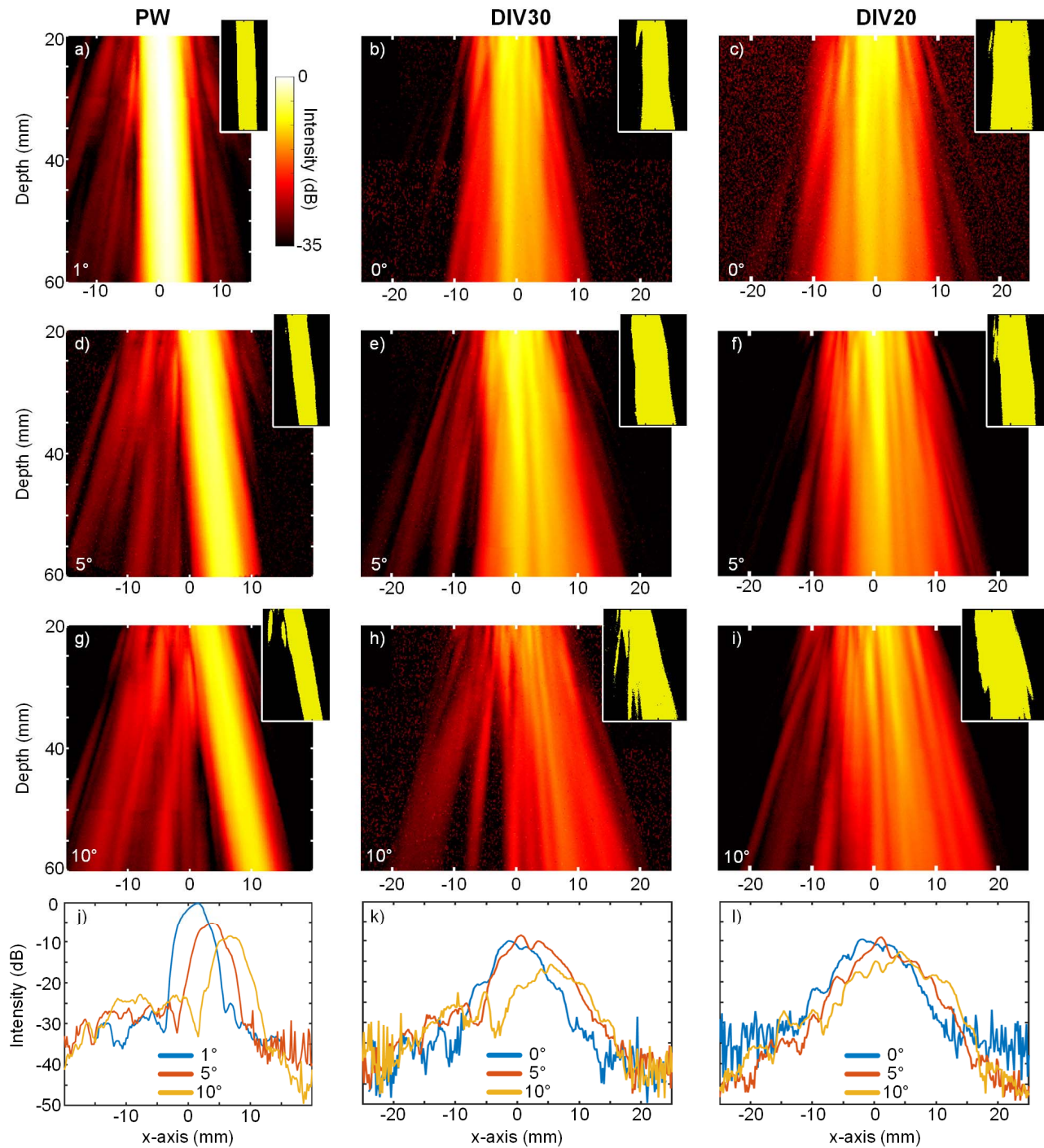
Movie 1  shows the wavefront propagation for the 1° steered PW as well as 0° steered DIV30 and DIV20 firings on the XZ plane as measured by the hydrophone. Here, it can be observed that the wavefront profile remains consistent as it propagates without any significant distortion in the main beam area (highlighted by the white borders). Outside of the main beam, the secondary lobe wavefront has an uneven and fluctuating profile as it propagates in all cases. Fig. 6(a)–(c) shows the snapshots from Movie 1  at three overlaid timepoints on each panel. The expected main beam profile is traced by the dotted lines and shows a close match to the measurements. Fig. 6(a)–(c) also shows that the wavefronts are followed by comet tails, which are secondary axial peaks that emerged as a result of using an element spacing larger than  $\lambda/2$  on the sparse array aperture. Such artifacts in the beam profile correspondingly give rise to axial image artifacts near echogenic image features. Movie 2  shows a similar wavefront propagation for the 10° steered firings of each type. Here, the main beam wavefront again remains coherent over its axial course of propagation. Fig. 6(d)–(f) shows the snapshots from the steered propagations and highlights the close match between the expected and measured profiles.

Fig. 7 plots the wavefront profiles at a 40 mm depth, including the expected, simulated, and measured profiles. Fig. 7(a), (d), and (g) shows the profiles for the PW firings, Fig. 7(b), (e), and (h) shows the profiles for the DIV30 firings, and Fig. 7(c), (f), and (i) shows the profiles for the DIV20 firings. Each row of Fig. 7 shows a different steering angle of the firing with the top row being 0/1°, the center row 5°, and the bottom row 10°. The RMSE values of the simulated and measured profiles are shown in the figure panels. From the PW profiles, the wavefronts are observed to have only minor deviations from the expected profile near the edges of the main beam where the intensity is lower. The DIV30 and DIV20 firings follow a similar trend with the center of the profile being the smoothest with increasing deviations toward the edges. Generally, the simulated data match slightly closer to the expected profile than the hydrophone data. However, in the case of the DIV20 firing, the simulated data show some deviation at the right and left sides of the plots due to the sparsity of elements at the edges of the array aperture and the widespread of the wavefront. In both the DIV30 and DIV20 firings, the hydrophone RMSE increases as the degree



**Fig. 4.** Intensity measurements for (a), (d), (g), and (j) PW; (b), (e), (h), and (k) DIV30; and (c), (f), (i), and (l) DIV20 for 0° and 1° steering (top row), 5° steering (second row), and 10° steering (third row). Insets in the top three rows of the figure show the beam intensity plots with a  $-12$ -dB threshold applied. Intensity profiles at 40 mm depth are shown in the bottom row overlaid for each steering angle to highlight the reduction in main beam intensity with steering coinciding with the increase in secondary lobe intensity.

of steering increases, which is not observed in the simulated data. The PW RMSE values are lower than the other firings and show smaller changes in RMSE between firing angles.

### C. Compounded Unfocused Firings Demonstrated High B-Mode Spatial Resolution With Limited Penetration Depth

B-mode images of a CIRS point target phantom (wire targets in 3-D) acquired with ten-angle compounded PW and DIV20

scans are shown in Fig. 8. Fig. 8(a) and (c) shows the B-mode slices on the  $x$ -axis of the array, which is perpendicular to the wires in the CIRS phantom. Fig. 8(b) and (d) shows the B-mode slices on the  $y$ -axis of the array that is parallel to the wires. In Fig. 8(a) and (b), the PW firings are able to resolve the wires to a depth of 22 mm with a lateral ( $x$ -axis) FWHM of 0.77 mm for the target at 12 mm depth and 0.89 mm for the target at 22 mm. The axial FWHM is 0.46 mm at 12 mm depth and 0.51 mm at 22 mm for PW. Fig. 8(c) and (d) shows

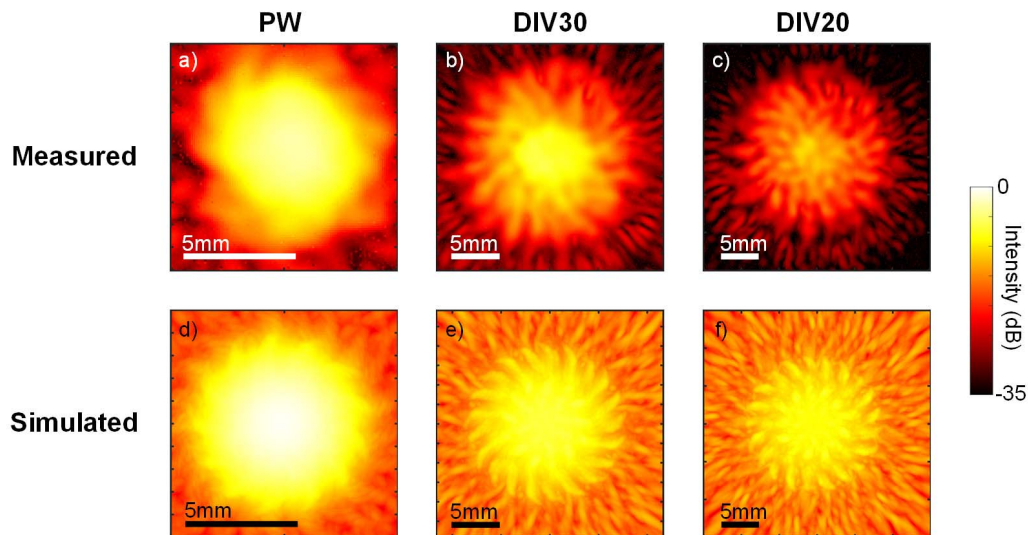


Fig. 5. Intensity measurements on XY planes at a depth of 40 mm in hydrophone experiments (top row) and simulation (bottom row) for (a) and (d) PW, (b) and (e) DIV30, and (c) and (f) DIV20.

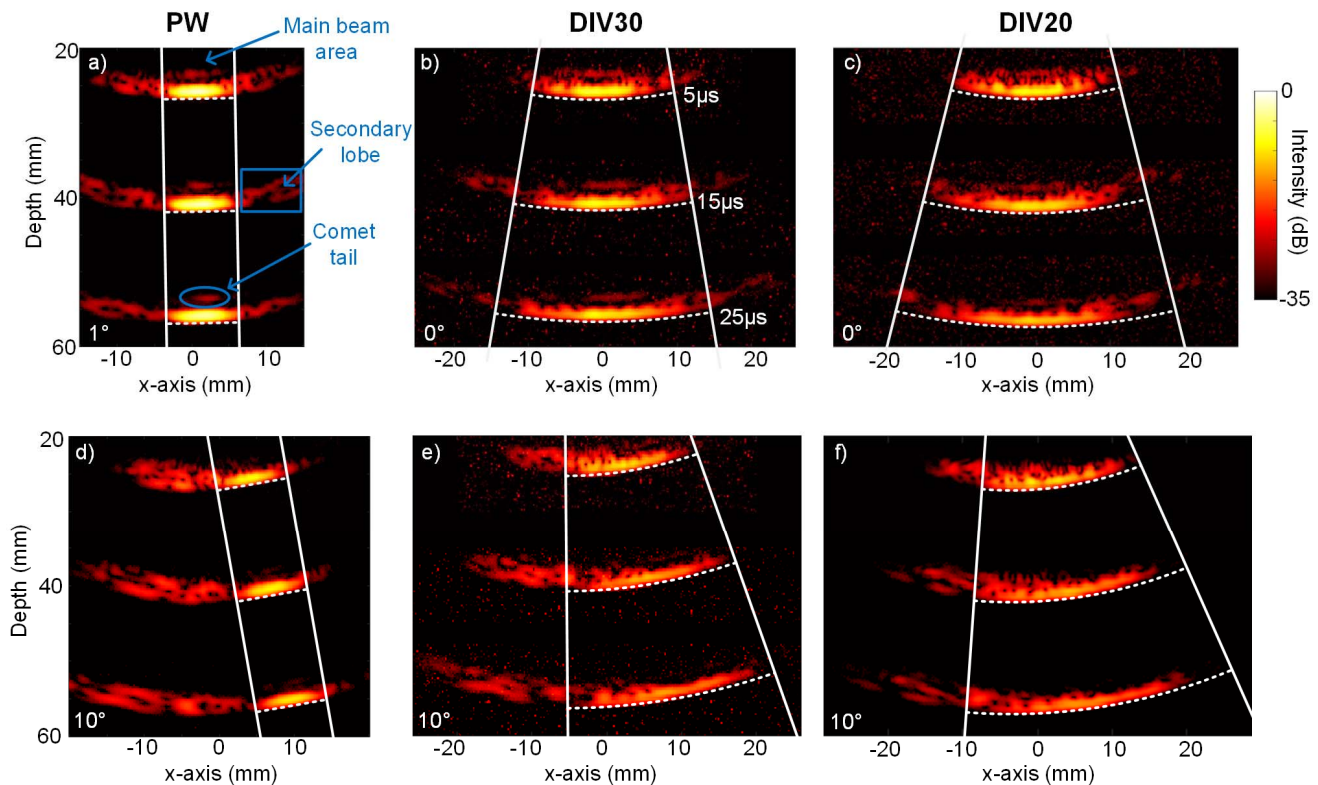
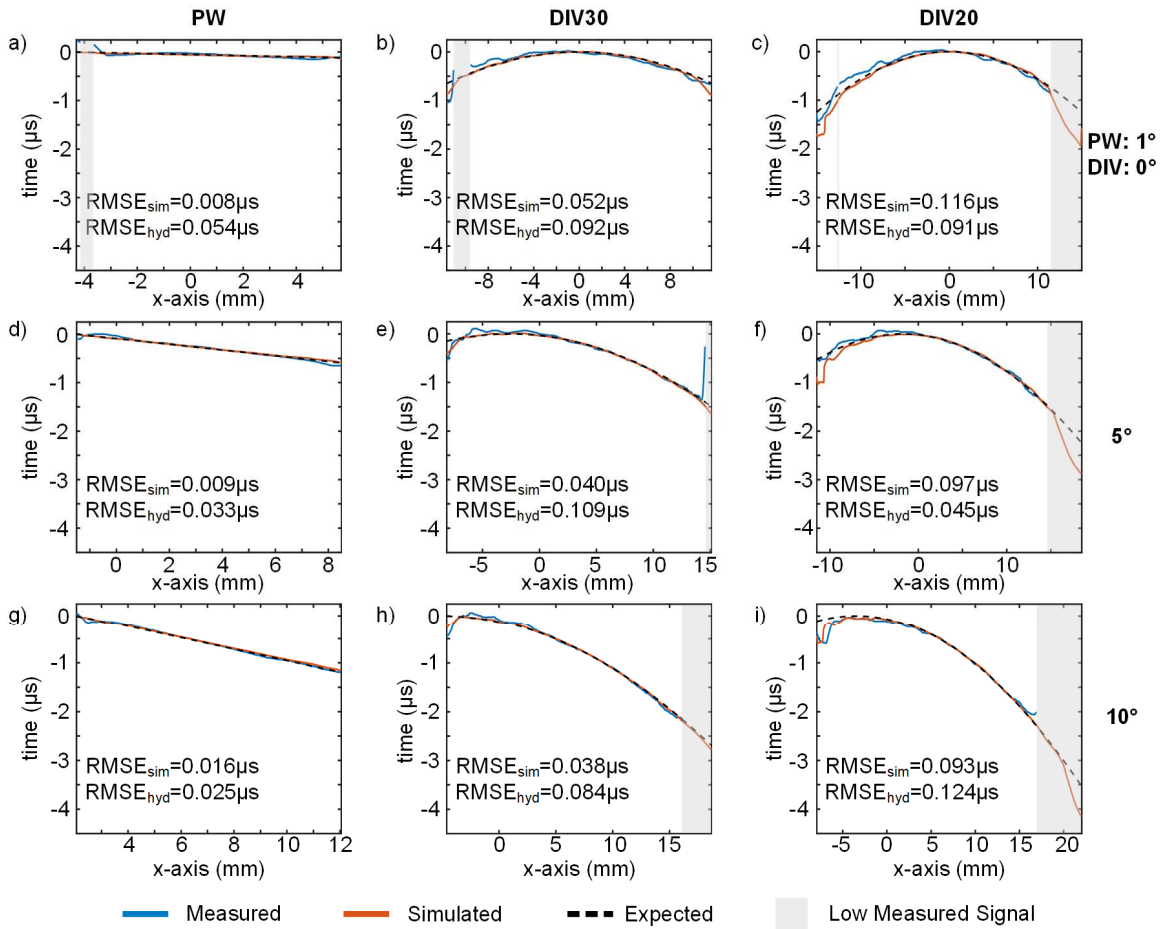


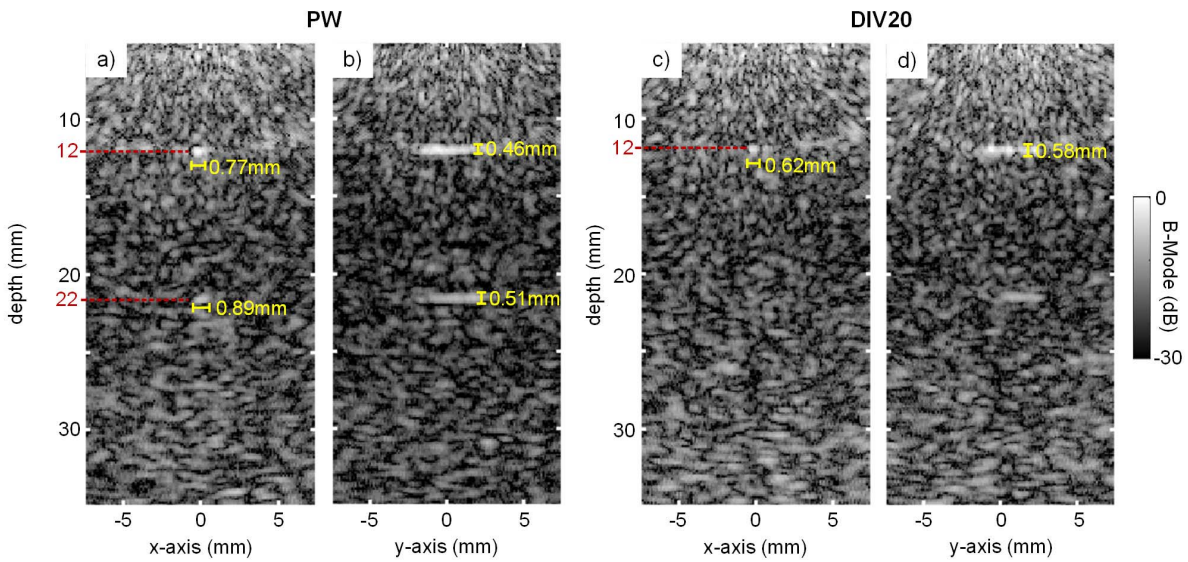
Fig. 6. Top row: overlaid stills from Movie 1 at 5, 15, and 25  $\mu\text{s}$  from the start of the acquisition on the oscilloscope for unsteered (a) PW, (b) DIV30, and (c) DIV20 firings. Solid white lines mark the edges of the theoretical main beam. Dashed white lines mark the expected wavefront profile. Bottom row: overlaid stills from Movie 2 at the same timepoints as the top row for (d) PW, (e) DIV30, and (f) DIV20 firings steered at  $10^\circ$ .

that the DIV20 firing was able to resolve the 12-mm target in the  $x$ - and  $y$  planes, but the 22-mm target is indistinguishable from the speckle pattern on the  $x$  plane and is only visible on the  $y$  plane. The lateral ( $x$ -axis) FWHM is 0.62 mm for the target at 12 mm depth and the axial FWHM is 0.58 mm for the same target.

Fig. 9 shows the B-mode images for the same PW and DIV20 scans on the wire target phantom immersed in water. Here, the targets were resolvable in both PW and DIV20 scans to a depth of 33 mm. In Fig. 9(a) and (b), the PW scans show a lateral FWHM of 0.60, 0.84, and 1.25 mm, respectively, for the 13-, 23-, and 33-mm depth targets. The axial FWHM on the



**Fig. 7.** Cross-sectional wavefront profiles for (a), (d), and (g) PW; (b), (e), and (h) DIV30; and (c), (f), and (i) DIV20 for 0° and 1° steering (top), 5° steering (middle), and 10° steering (bottom) at a depth of 40 mm. RMSE values calculated for the simulated and hydrophone profiles are shown as insets. Gray bars indicate regions where the voltage read from the hydrophone was within 2 mV of the noise floor, and therefore, the wavefront could not be accurately identified. These regions were omitted in all RMSE calculations.



**Fig. 8.** B-mode images of point targets in a CIRS phantom formed by the coherent compounding of ten unfocused transmissions (steering from  $-5^\circ$  to  $5^\circ$  along the x-axis). (a) PW image of XZ plane at  $y = 0$ . (b) PW image of YZ plane at  $x = 0$ . (c) DIV20 image of XZ plane at  $y = 0$ . (d) DIV20 image of YZ plane at  $x = 0$ .

same targets are 0.47, 0.44, and 0.47 mm. In Fig. 9(c) and (d), the DIV20 scans produced the lateral FWHM of 0.61, 0.90, and 1.45 mm for the 13-, 23-, and 33-mm target depths along with the axial FWHM of 0.50, 0.49, and 0.46 mm, respectively. Generally, the FWHM results of the water-based phantom align with those on the CIRS phantom. A notable difference



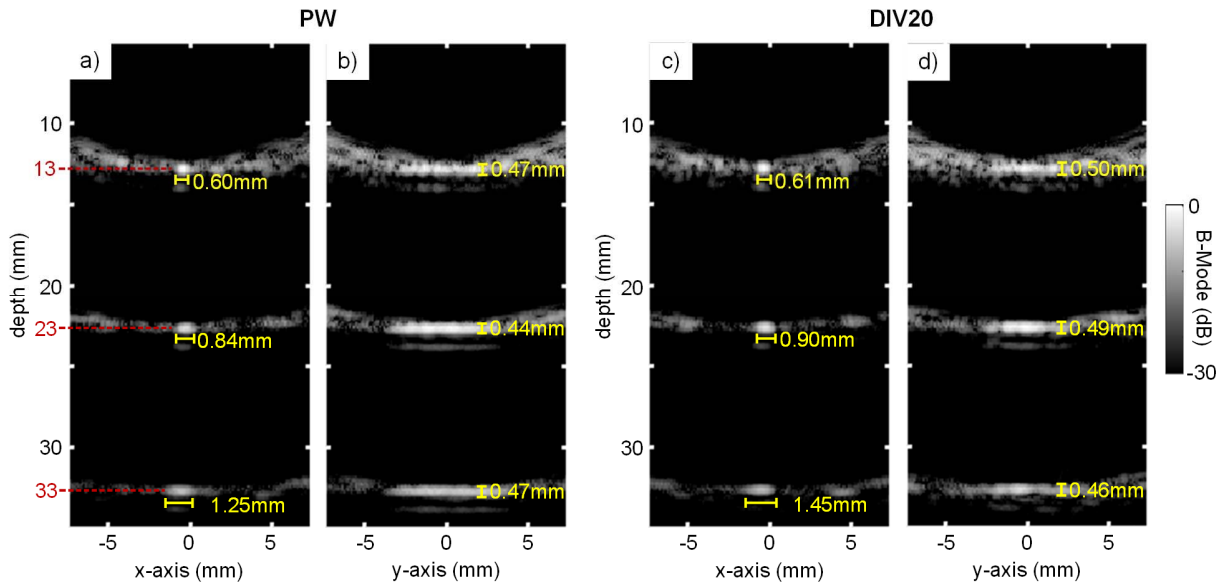


Fig. 9. B-mode images of point targets in an in-house made wire target phantom immersed in water formed by the coherent compounding of ten unfocused transmissions (steering from  $-5^\circ$  to  $5^\circ$  along the x-axis). (a) PW image of XZ plane at  $y = 0$ . (b) PW image of YZ plane at  $x = 0$ . (c) DIV20 image of XZ plane at  $y = 0$ . (d) DIV20 image of YZ plane at  $x = 0$ .

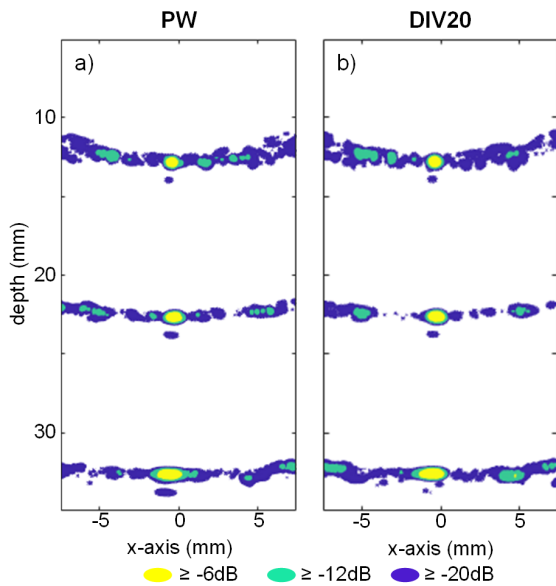


Fig. 10. Contour plots of the B-mode images of the point targets in water for (a) PW scan [Fig. 9(a)] and (b) DIV20 scan [Fig. 9(c)] with thresholds of  $-20$ ,  $-12$ , and  $-6$  dB to highlight the sidelobe intensity levels.

in the measurements is the presence of the secondary lobes, which is much more apparent with the hypoechoic background of the water-based phantom. For the PW scan, the average SLL was  $-19.46$ ,  $-20.87$ , and  $-24.87$  dB for the 13-, 23-, and 33-mm depth targets, respectively. For the DIV20 scan, the average SLL was  $-19.37$ ,  $-22.91$ , and  $-21.29$  dB. Fig. 10 shows a contour plot of the ZX plane B-mode images in Fig. 9 with intensity thresholds of  $-20$ ,  $-12$ , and  $-6$  dB. The secondary lobes are normalized to the peak value of their adjacent point target. Fig. 10(a) shows the PW scan where the majority of the secondary lobes are between  $-20$  and  $-12$  dB. There are, however, localized pockets of higher secondary

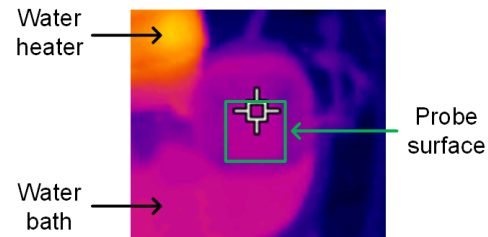


Fig. 11. Infrared image of the probe surface acquired after 30 min of continuous transmission.

lobe intensity that surpass  $-12$  dB. Fig. 10(b) shows a similar representation for the DIV20 scan.

#### D. Surface Temperature and Acoustic Exposure Levels Are Within Regulatory Limits



The surface temperature of the density-tapered spiral array was found to be  $30.2 \text{ }^\circ\text{C} \pm 0.7 \text{ }^\circ\text{C}$  ( $\pm$  one standard deviation) after 30 min of continuous transmission. This temperature is below  $43 \text{ }^\circ\text{C}$  limit set forth by IEC 60601-2-37 [21]. Fig. 11 shows an infrared image of the probe surface. The probe temperature was observed to be uniform across the entire surface.

Based on the established acoustic exposure formulas [27], the spatial-peak, pulse-average (SPPA) intensity and mechanical index (MI) of the PW mode were, respectively,  $0.298 \text{ W/cm}^2$  and  $0.034$  for a maximum unfocused PNP of  $93.9 \text{ kPa}$  (Section III-A). For DIV30 and DIV20 that had the maximum measured PNP of  $59.3$  and  $45.6 \text{ kPa}$ , respectively (Section III-A), the corresponding SPPA intensity was  $0.119$  and  $0.070 \text{ W/cm}^2$ , while the MI was  $0.022$  and  $0.017$ , respectively. All the intensities and MI values reported here are below FDA's emission limits for diagnostic imaging [21].

## IV. DISCUSSION

### A. Statement of Contributions

This work presents a detailed study of unfocused transmission characteristics from the density-tapered spiral array to evaluate its viability in facilitating high-volume-rate 3-D ultrasound imaging. In principle, the use of a spiral array to facilitate 3-D imaging eliminates the need for expensive scanner hardware modifications and provides flexibility in imaging mode development. While the spiral array has previously been studied in focused firings [22], here, we study unfocused transmissions that are essential to realizing high-volume-rate 3-D imaging, particularly for transmissions involving multicycle pulses that are required to perform flow mapping.

In our investigation, three acoustic field properties of unfocused firings have been evaluated for the spiral array: 1) beam intensity; 2) wavefront arrival time profile; and 3) B-mode image quality. Fig. 4 highlights the uniformity of the unfocused beam intensity within the main beam region as well as demonstrates the relatively low secondary lobe intensity compared to the main beam. Movies 1  and 2  show that, despite the low element density, the wavefront profile remains smooth throughout propagation, while Fig. 7 shows that the wavefronts have only small deviations from the expected profiles. Together, these results indicate that the array's sparsity does not dramatically impact wavefront shape. Figs. 8 and 9 present the first compounded PW and diverging-wave images from the density-tapered spiral array, which shows promising spatial resolution. Yet, penetration depth remains limited, suggesting a need for the development of signal enhancement strategies (to be discussed in Section IV-C).

Another component of this investigation is an experimental analysis of the spiral array's exposure safety when it operates under unfocused transmission modes. The maximum unfocused PNP measured by the hydrophone was 93.9 kPa (Section III-A), while the highest SPPA intensity and MI were, respectively, 0.298 W/cm<sup>2</sup> and 0.034 (Section III-D). These exposure values are well within FDA's regulatory limits for imaging [21]. Also, the entire array exhibited a homogeneous surface temperature distribution (Fig. 11) with an average temperature (30.2 °C ± 0.7 °C) that is well below the IEC requirement of 43 °C after 30 min of continuous imaging [21]. These results confirm that the spiral array does not pose acoustic exposure concerns when it operates in unfocused transmission modes.

### B. Summative Interpretation of Findings

Our investigation has generally attested that the density-tapered spiral array can produce unfocused transmissions with the desired field profile characteristics. Specifically, the main beam of the unfocused transmissions had a smooth intensity profile without large fluctuations. Such a smooth beam profile signifies that the propagation of the main wavefront is homogeneous and dispersion is limited. The main beam also had a radially uniform pressure field. One minor irregularity to be noted is that, for diverging waves, the peak of the main wavefront was not laterally centered against the angle

steering axis. This issue can be observed in Fig. 4(k) and (l) that plot the  $x$ -axis field intensities at 40 mm depth for steering angles of 0°, 5°, and 10°; for instance, the main peak was not located at the  $x$ -axis origin for 0° steering. Such a field characteristic is likely attributed to the sparse positioning of spiral array elements that resulted in the generation of anomalous interference patterns on the main wavefront as it propagates across depth. Nevertheless, it is after all not a serious issue since the main wavefront remained laterally homogeneous with deviations within 3 dB.

From an imaging perspective, the field characteristics generated from the spiral array favor homogeneous insonation of the image volume, which is desirable for volumetric pulse-echo sensing. While secondary lobes are present in the firings due to the  $>\lambda/2$  element spacing, their intensity is below the -12 dB threshold relative to the main beam peak in nearly all observed cases. The relatively low secondary lobe intensity is due to the nongridDED element layout of the density tapered spiral array, which prevents strong constructive interference outside of the main beam as is present when regular gridded sparse arrays are used [15], [16].

The secondary lobes from the spiral array are expected to have a limited impact on imaging performance unless steering of more than 10° is applied, which is generally not required for multi-angle Doppler flow estimation [23]. For instance, as demonstrated in the B-mode images of Fig. 8 which used -5° to +5° steering, adjacent to the point targets, we did not observe echogenic artifacts that are attributed to secondary lobes. In the B-mode images of Fig. 9, the average SLLs were all found to be below -19 dB with only small local regions above -12 dB. For Doppler flow imaging, secondary lobes may lead to errors in the mean Doppler frequency estimation process since these lobes may spatially encompass nearby vessels with flow characteristics different from that in the main sample volume. Nevertheless, with the relatively low SLL magnitudes observed in Fig. 9, the weighted impact of these secondary lobes on mean Doppler estimation is expected to be limited.

This work, combined with previous works on focused beams [22], demonstrates the promising acoustic field profile performance of the spiral array layout. Although the spiral array's field profile characteristics are less desirable than those for a fully populated 2-D matrix array, the significant reduction in the spiral array's element count is an important factor that favors its integration with ultrasound scanners designed for 2-D imaging. Note that the measured peak pressure value is lower than typical PW transmissions from PZT arrays. Some pressure reduction is to be expected from 2-D arrays due to the lack of elevation focusing, but in this case, the CMUT architecture of the array is also likely a contributing factor. CMUT arrays generally have limited transmission sensitivity. Moreover, the CMUT array used in this study suffered from a high parasitic capacitance introduced by the "dummy" (passive) ASIC used to route the element signals, as described in [22], resulting in poor signal strength for the array during imaging. The B-mode images presented in this work show a penetration depth of just 1–2 cm confirming the low signal levels. Increasing the bias voltage of the array elements may

enhance the signal strength, but this risks permanent damage to the array elements. Therefore, alternative means of increasing the transmit and receive signals must be investigated (to be discussed in Section IV-C).

### C. Limitations and Future Work

Although the density-tapered spiral array has yielded favorable acoustic field patterns for unfocused transmissions, it is subject to some notable limitations that should be addressed. As mentioned in Section IV-B, signal strength needs to be enhanced to increase the effective imaging depth when using unfocused transmissions for imaging. On this topic, three directions of investigation are worth pursuing: 1) the design of coded excitation schemes; 2) the development of PZT-based spiral arrays; and 3) the development of CMUT arrays with enhanced interconnection strategies. For the first direction, the CMUT spiral array is an excellent candidate for the implementation of coded excitation imaging schemes due to its wideband nature, which enables the transmission of various codes, including chirps. Recently, chirp transmissions have been shown to increase the Doppler SNR making them a potential candidate to improve high-volume-rate 3-D imaging [28]. However, when wideband transmissions such as chirps are used for flow estimation, a large estimation variance occurs. Therefore, to implement chirps for dynamic flow imaging, future works should focus on novel methods to reduce the flow estimation variance.

For the second future research direction, the use of a PZT array architecture can effectively reduce the SNR loss related to parasitic capacitance and the transmission sensitivity issue that CMUT arrays are susceptible to. Previous work has shown that a PZT sparse array can produce high-quality diverging wave images [29], although a lower transmission frequency of 3 MHz was used, which naturally improves penetration according to ultrasound physics. The main drawback of the PZT architecture is that the arrays are currently limited to gridded layouts making the true density tapered spiral design not possible to exactly replicate [30]. Thus, there is a tradeoff between the PZT and CMUT versions of the spiral array design where PZT produces higher signal levels in transmit and receive, while CMUT demonstrates an improved secondary lobe performance. The considerations required to assess this tradeoff are nontrivial and will likely necessitate a more direct comparison of the two technologies in the future.

The third research direction on designing CMUT arrays with enhanced interconnection strategies would lower the parasitic capacitance. In turn, these arrays would expectedly reduce the attenuation of the received signals. In addition, the array can be integrated with low-noise amplifiers connected as close as possible to the array elements to minimize the capacitance, such as the alternative version of the array described previously [22].

Besides the need to enhance signal strength, the spiral array's small physical aperture (0.6 cm effective diameter) is another technical limitation to be noted. While it may be tempting to increase the array aperture beyond its current size while maintaining the frequency characteristics of the array, doing so would result in stronger secondary lobes as the spar-

ity of the element distribution would increase. Lowering the center frequency of the array (thereby increasing  $\lambda$ ) could mitigate the increase in secondary lobe level. Nevertheless, such an approach would naturally degrade the spatial resolution.

It is worth noting that such a physical size limitation is not unique to the density-tapered spiral array used in this work, as other 2-D arrays currently under development have similar dimensions (see [28]). Yet, the limited aperture is particularly problematic in unfocused imaging studies where the compounding of multiple transmissions is required to achieve good imaging performance. Since the aperture is small, the region of overlap between oppositely steered PW transmissions is quite limited, thereby reducing the number of unique transmissions that can be used to resolve a specific region. For example, the B-mode images presented in this work include only  $-5^\circ$  to  $5^\circ$  steering since higher degrees of steering for PWs no longer intersect with the point targets as they would with wider aperture arrays. To a certain extent, the use of diverging waves can help to mitigate this issue, but the resulting field pressure magnitude is lower than that of PWs and the penetration depth becomes more limited.

## V. CONCLUSION

In the development of 3-D ultrasound systems, spiral arrays with a sparse 2-D aperture have been investigated as a transducer front end that can acquire volumetric data at rates similar to 2-D imaging. However, they have yet to be investigated for their unfocused field properties and potential in high-volume-rate imaging. To fill this knowledge gap, this article has presented a detailed analysis of the unfocused firing characteristics of a density-tapered spiral array and observed smooth wavefront profiles and negligible secondary lobe characteristics. Since the wavefront profile was found to be consistent and predictable, there is little delay difference from a fully populated array making existing beamforming strategies readily portable to this array. This statement is underscored by the good spatial resolution observed in the presented B-mode images formed using delay-and-sum beamforming (even though penetration depth was limited). Sparse arrays, such as the density-tapered spiral array, coupled with unfocused transmissions, provide a viable means of acquiring high-volume-rate 3-D imaging data without the need for a massive system with over 1000 channels of transceiver electronics. With these arrays, high-volume-rate 3-D imaging can potentially be realized on 2-D imaging systems and, in turn, be mobilized for use at a broader scale.

## REFERENCES

- [1] S. Holbek, T. L. Christiansen, M. B. Stuart, C. Beers, E. V. Thomsen, and J. A. Jensen, "3-D vector flow estimation with row-column-addressed arrays," *IEEE Trans. Ultrason., Ferroelectr., Freq. Control*, vol. 63, no. 11, pp. 1799–1814, Nov. 2016.
- [2] M. Correia, J. Provost, M. Tanter, and M. Pernot, "4D ultrafast ultrasound flow imaging: In vivo quantification of arterial volumetric flow rate in a single heartbeat," *Phys. Med. Biol.*, vol. 61, no. 23, pp. L48–L61, Nov. 2016.
- [3] A. Fenster, D. B. Downey, and H. N. Cardinal, "Three-dimensional ultrasound imaging," *Phys. Med. Biol.*, vol. 46, no. 5, pp. R67–R99, Apr. 2001.

- [4] O. T. von Ramm and S. W. Smith, "Real time, volumetric ultrasound imaging system," *J. Digit. Imag.*, vol. 3, no. 4, pp. 261–268, Nov. 1990.
- [5] P. R. Hoskins, "Haemodynamics and blood flow measured using ultrasound imaging," *Proc. Inst. Mech. Eng. H, J. Eng. Med.*, vol. 224, no. 2, pp. 255–271, Feb. 2010.
- [6] J. A. Jensen, S. I. Nikolov, A. C. H. Yu, and D. Garcia, "Ultrasound vector flow imaging—Part I: Sequential systems," *IEEE Trans. Ultrason., Ferroelectr., Freq. Control*, vol. 63, no. 11, pp. 1704–1721, Nov. 2016.
- [7] J. A. Jensen, S. I. Nikolov, A. C. H. Yu, and D. Garcia, "Ultrasound vector flow imaging—Part II: Parallel systems," *IEEE Trans. Ultrason., Ferroelectr., Freq. Control*, vol. 63, no. 11, pp. 1722–1732, Nov. 2016.
- [8] L. Petrusca *et al.*, "Fast volumetric ultrasound B-mode and Doppler imaging with a new high-channels density platform for advanced 4D cardiac imaging/therapy," *Appl. Sci.*, vol. 8, no. 2, p. 200, Jan. 2018.
- [9] E. Boni *et al.*, "ULA-OP 256: A 256-channel open scanner for development and real-time implementation of new ultrasound methods," *IEEE Trans. Ultrason., Ferroelectr., Freq. Control*, vol. 63, no. 10, pp. 1488–1495, Oct. 2016.
- [10] J. A. Jensen *et al.*, "SARUS: A synthetic aperture real-time ultrasound system," *IEEE Trans. Ultrason., Ferroelectr., Freq. Control*, vol. 60, no. 9, pp. 1838–1852, Sep. 2013.
- [11] C. E. Morton and G. R. Lockwood, "Theoretical assessment of a crossed electrode 2-D array for 3-D imaging," in *Proc. IEEE Symp. Ultrason.*, Honolulu, HI, USA, Oct. 2003, pp. 968–971.
- [12] C. E. M. Demore, A. W. Joyce, K. Wall, and G. R. Lockwood, "Real-time volume imaging using a crossed electrode array," *IEEE Trans. Ultrason., Ferroelectr., Freq. Control*, vol. 56, no. 6, pp. 1252–1261, Jun. 2009.
- [13] G. R. Lookwood and F. S. Foster, "Optimizing the radiation pattern of sparse periodic two-dimensional arrays," *IEEE Trans. Ultrason., Ferroelectr., Freq. Control*, vol. 43, no. 1, pp. 15–19, Jan. 1996.
- [14] A. Trucco, "Thinning and weighting of large planar arrays by simulated annealing," *IEEE Trans. Ultrason., Ferroelectr., Freq. Control*, vol. 46, no. 2, pp. 347–355, Mar. 1999.
- [15] J. T. Yen, J. P. Steinberg, and S. W. Smith, "Sparse 2-D array design for real time rectilinear volumetric imaging," *IEEE Trans. Ultrason., Ferroelectr., Freq. Control*, vol. 47, no. 1, pp. 93–110, Jan. 2000.
- [16] A. Austeng and S. Holm, "Sparse 2-D arrays for 3-D phased array imaging—design methods," *IEEE Trans. Ultrason., Ferroelectr., Freq. Control*, vol. 49, no. 8, pp. 1073–1086, Aug. 2002.
- [17] O. Martínez-Graullera, C. J. Martín, G. Godoy, and L. G. Ullate, "2D array design based on Fermat spiral for ultrasound imaging," *Ultrasonics*, vol. 50, no. 2, pp. 280–289, Feb. 2010.
- [18] B. Diarra, M. Robini, P. Tortoli, C. Cachard, and H. Liebgott, "Design of optimal 2-D nongrid sparse arrays for medical ultrasound," *IEEE Trans. Biomed. Eng.*, vol. 60, no. 11, pp. 3093–3102, Nov. 2013.
- [19] A. Ramalli, E. Boni, A. S. Savoia, and P. Tortoli, "Density-tapered spiral arrays for ultrasound 3-D imaging," *IEEE Trans. Ultrason., Ferroelectr., Freq. Control*, vol. 62, no. 8, pp. 1580–1588, Aug. 2015.
- [20] E. Roux, A. Ramalli, P. Tortoli, C. Cachard, M. Robini, and H. Liebgott, "2-D ultrasound sparse arrays multidepth radiation optimization using simulated annealing and spiral-array inspired energy functions," *IEEE Trans. Ultrason., Ferroelectr., Freq. Control*, vol. 63, no. 12, pp. 2138–2149, Dec. 2016.
- [21] F. A. Duck, "Medical and non-medical protection standards for ultrasound and infrasound," *Progr. Biophys. Mol. Biol.*, vol. 93, nos. 1–3, pp. 176–191, 2007.
- [22] A. S. Savoia *et al.*, "A 256-element spiral CMUT array with integrated analog front end and transmit beamforming circuits," in *Proc. IEEE Ultrason. Symp.*, Kobe, Japan, Oct. 2018, pp. 206–212.
- [23] B. Y. S. Yiu and A. C. H. Yu, "Least-squares multi-angle Doppler estimators for plane-wave vector flow imaging," *IEEE Trans. Ultrason., Ferroelectr., Freq. Control*, vol. 63, no. 11, pp. 1733–1744, Nov. 2016.
- [24] J. A. Jensen and N. B. Svendsen, "Calculation of pressure fields from arbitrarily shaped, apodized, and excited ultrasound transducers," *IEEE Trans. Ultrason., Ferroelectr., Freq. Control*, vol. 39, no. 2, pp. 262–267, Mar. 1992.
- [25] J. A. Jensen, "Field: A program for simulating ultrasound systems," *Med. Biol. Eng. Comput.*, vol. 34, no. 1, pp. 351–353, 1997.
- [26] B. Y. S. Yiu, I. K. H. Tsang, and A. C. H. Yu, "GPU-based beamformer: Fast realization of plane wave compounding and synthetic aperture imaging," *IEEE Trans. Ultrason., Ferroelectr., Freq. Control*, vol. 58, no. 8, pp. 1698–1705, Aug. 2011.
- [27] X. Duan, A. C. H. Yu, and J. M. F. Wan, "Cellular bioeffect investigations on low-intensity pulsed ultrasound and sonoporation: Platform design and flow cytometry protocol," *IEEE Trans. Ultrason., Ferroelectr., Freq. Control*, vol. 66, no. 9, pp. 1422–1434, Sep. 2019.
- [28] A. Ramalli *et al.*, "Real-time 3-D spectral Doppler analysis with a sparse spiral array," *IEEE Trans. Ultrason., Ferroelectr., Freq. Control*, vol. 68, no. 5, pp. 1742–1751, May 2021.
- [29] E. Roux, F. Varray, L. Petrusca, C. Cachard, P. Tortoli, and H. Liebgott, "Experimental 3-D ultrasound imaging with 2-D sparse arrays using focused and diverging waves," *Sci. Rep.*, vol. 8, Jun. 2018, Art. no. 9108.
- [30] E. Roux, A. Ramalli, H. Liebgott, C. Cachard, M. C. Robini, and P. Tortoli, "Wideband 2-D array design optimization with fabrication constraints for 3-D US imaging," *IEEE Trans. Ultrason., Ferroelectr., Freq. Control*, vol. 64, no. 1, pp. 108–125, Jan. 2017.



**Rebekah Maffett** (Graduate Student Member, IEEE) received the B.A.Sc. degree in nanotechnology engineering from the University of Waterloo, Waterloo, ON, Canada, in 2018, where she is currently pursuing the Ph.D. degree in electrical and computer engineering.

She has been a member of the Laboratory on Innovative Technology in Medical Ultrasound (LITMUS), University of Waterloo, since 2018. Her research interests are in the design of vascular ultrasound techniques leveraging new 3-D ultrasound technologies.

Ms. Maffett was a recipient of the NSERC Postgraduate Scholarship and the UW Engineering Excellence Fellowship.



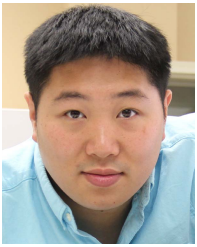
**Enrico Boni** (Senior Member, IEEE) was born in Florence, Italy, in 1977. He graduated in electronic engineering from the University of Florence, Florence, Italy, in 2001. He received the Ph.D. degree in electronic system engineering from the University of Florence in 2005.

Since December 2021, he has been an Associate Professor in electronics with the Department of Information Engineering, University of Florence. His research interests include analog and digital systems design, digital signal processing algorithms, digital control systems, Doppler ultrasound signal processing, microemboli detection and classification, ultrasound research platforms, and ultrasound frontend electronics design.



**Adrian J. Y. Chee** (Member, IEEE) received the B.Eng. degree in electrical and computer systems engineering from Monash University, Melbourne, VIC, Australia, in 2011, and the Ph.D. degree in mechanical engineering from The University of Hong Kong, Hong Kong, in 2016.

He was a Corporate Intern at the Hitachi Central Research Laboratory, Tokyo, Japan, in 2016. He is currently an Associate Scientist with the Laboratory on Innovative Technology in Medical Ultrasound, University of Waterloo, Waterloo, ON, Canada. His research interests are in designing new vascular ultrasound techniques and related experimental tools.



**Billy Y. S. Yiu** (Member, IEEE) received the B.Eng. degree (Hons.) in medical engineering and the M.Phil. degree in electrical and electronic engineering from The University of Hong Kong, Hong Kong, in 2007 and 2010, respectively, and the Ph.D. degree in electrical and computer engineering from the University of Waterloo, Waterloo, ON, Canada, in 2019.

Before joining the University of Waterloo, he was a Research Staff with the Biomedical Ultrasound Laboratory, The University of Hong Kong, from 2010 to 2016. He is currently a Research Assistant Professor and the Co-Principal Investigator with the Laboratory on Innovative Technology in Medical Ultrasound (LITMUS), University of Waterloo. His research interests are in advanced ultrasound imaging techniques and systems.

Dr. Yiu was a past recipient of the USE Young Scientist Award, the KSUM Young Investigator Gold Prize Award, and the ASA Biomedical Acoustics Best Student Paper Award.



**Alessandro Stuart Savoia** (Member, IEEE) received the Laurea (M.S.) and Ph.D. degrees in electronic engineering from Roma Tre University, Rome, Italy, in 2003 and 2007, respectively.

He leads the ultrasonic transducers research activities at the Acoustoelectronics Laboratory, Department of Industrial, Electronic, and Mechanical Engineering, Roma Tre University. His research interests are mainly focused on the development and system integration of MEMS ultrasonic transducers [capacitive micro-

machined ultrasound transducer (CMUT) and piezoelectric micromachined ultrasound transducer (PMUT)].

Dr. Savoia serves the UFFC Society as an Associate Editor for the IEEE TRANSACTIONS ON ULTRASONICS, FERROELECTRICS AND FREQUENCY CONTROL since 2017, the Co-Chair of the TPC Group 5 "Transducers and Transducer Materials" for the International Ultrasonics Symposium since 2018, and an Elected Member for AdCom since 2021.



**Alessandro Ramalli** (Senior Member, IEEE) was born in Prato, Italy, in 1983. He received the master's degree in electronics engineering from the University of Florence, Florence, Italy, in 2008, and the joint Ph.D. degree in electronics system engineering and in automation, systems and images from the University of Florence and the University of Lyon, Lyon, France, in 2012.

From 2012 to 2017, he was involved in the development of the imaging section of a programmable open ultrasound system at the University

of Florence. From 2017 to 2019, he worked as a Postdoctoral Researcher with the Laboratory of Cardiovascular Imaging and Dynamics, KU Leuven, Leuven, Belgium, granted by the European Commission through a "Marie Skłodowska-Curie Individual Fellowship." Here, he developed high-frame-rate imaging techniques for echocardiography. From 2020 to 2022, he worked as a Research Fellow with the University of Florence, where he is currently an Assistant Professor. His research interests include medical imaging, echocardiography, beamforming methods, ultrasound simulation, arrays, and systems design.



**Piero Tortoli** (Fellow, IEEE) received the Laurea degree in electronics engineering from the University of Florence, Florence, Italy, in 1978.

Since 1978, he has been on the faculty of the Department of Information Engineering, University of Florence, where he is currently a Full Professor of electronics. He is leading the Microelectronics Systems Design Laboratory at the University of Florence. His research interests include the development of open ultrasound research systems and novel imaging/Doppler methods. On these topics, he has authored more than 300 articles.

Prof. Tortoli was an elected member of the Academic Senate. He is a fellow of AIMBE, the "Docteur Honoris causa" of the University Claude Bernard Lyon 1, and an Honorary Member of the Polish Academy of Sciences. He has served on the IEEE International Ultrasonics Symposium Technical Program Committee since 1999. He was an Associate Editor and a Guest Editor for three special issues of the IEEE TRANSACTIONS ON ULTRASONICS, FERROELECTRICS, AND FREQUENCY CONTROL from 2013 to 2022 and in 2006, 2016, and 2018, respectively. He chaired the 22nd International Symposium on Acoustical Imaging in 1995 and the 12th New England Doppler Conference in 2003, established the Artimino Conference on Medical Ultrasound Technology in 2011, and organized it again in 2017.



**Alfred C. H. Yu** (Senior Member, IEEE) received the B.Sc. degree in electrical engineering from the University of Calgary, Calgary, AB, Canada, in 2002, and the M.A.Sc. and Ph.D. degrees in biomedical engineering from the University of Toronto, Toronto, ON, Canada, in 2004 and 2007, respectively.

From 2007 to 2015, he was the Founding Principal Investigator of the Biomedical Ultrasound Laboratory, The University of Hong Kong, Hong Kong. In 2015, he relocated to the University of Waterloo, Waterloo, ON, Canada. He is currently a Professor of biomedical engineering with the University of Waterloo, where he is also the Director of the Laboratory on Innovative Technology in Medical Ultrasound (LITMUS). He is also the Director of the Natural Sciences and Engineering Research Council of Canada (NSERC) Collaborative Research Training Program on "Next-Generation Innovations in Ultrasonics" in Canada. He has long-standing research interests in ultrasound imaging and therapeutics.

Dr. Yu has been named as a Steacie Fellow by NSERC. He is a fellow of the American Institute of Ultrasound in Medicine. Earlier in his career, he was a recipient of the IEEE Ultrasonics Early Career Investigator Award, the Frederic Lizzi Award, and the Ontario Early Researcher Award. He was the past Chair of the Medical Ultrasound Group of the IEEE Ultrasonics Symposium and was an Elected AdCom Member of the IEEE UFFC Society. He is currently the Editor-in-Chief of the IEEE TRANSACTIONS ON ULTRASONICS, FERROELECTRICS, AND FREQUENCY CONTROL.